PCCP

PAPER

View Article Online
View Journal | View Issue

Cite this: *Phys. Chem. Chem. Phys.*, 2018, **20**, 2457

Photodissociation dynamics of acetone studied by time-resolved ion imaging and photofragment excitation spectroscopy

Benjamin W. Toulson, † Dmitry A. Fishman and Craig Murray *

The photodissociation dynamics of acetone has been investigated using velocity-map ion imaging and photofragment excitation (PHOFEX) spectroscopy across a range of wavelengths spanning the first absorption band (236–308 nm). The radical products of the Norrish Type I dissociation, methyl and acetyl, as well as the molecular product ketene have been detected by single-photon VUV ionization at 118 nm. Ketene appears to be formed with non-negligible yield at all wavelengths, with a maximum value of $\Phi \approx 0.3$ at 280 nm. The modest translational energy release is inconsistent with dissociation over high barriers on the S_0 surface, and ketene formation is tentatively assigned to a roaming pathway involving frustrated dissociation to the radical products. Fast-moving radical products are detected at $\lambda \leq 305$ nm with total translational energy distributions that extend to the energetic limit, consistent with dissociation occurring near-exclusively on the T_1 surface following intersystem crossing. At energies below the T_1 barrier a statistical component indicative of S_0 dissociation is observed, although dissociation *via* the S_1/S_0 conical intersection is absent at shorter wavelengths, in contrast to acetaldehyde. The methyl radical yield is enhanced over that of acetyl in PHOFEX spectra at $\lambda \leq 260$ nm due to the onset of secondary dissociation of internally excited acetyl radicals. Time-resolved ion imaging experiments using picosecond duration pulses at 266 nm find an appearance time constant of $\tau = 1490 \pm 140$ ps for CH_3 radicals formed on T_1. The associated rate is representative of $S_1 \rightarrow T_1$ intersystem crossing. At 284 nm, CH_3 is formed on T_1 with two distinct timescales: a fast <10 ns component is accompanied by a slower component with $\tau = 42 \pm 7$ ns. A two-step mechanism involving fast internal conversion, followed by slower intersystem crossing ($S_1 \rightarrow S_0 \rightarrow T_1$) is proposed to explain the slow component.

Received 29th October 2017,
Accepted 29th December 2017

DOI: 10.1039/c7cp07320h

rsc.li/pccp

Introduction

Acetone (CH_3COCH_3) is the simplest ketone and its photodissociation is arguably one of the best studied photochemical reactions. Interest in the photochemistry and photophysics of acetone has been driven in part by its role in atmospheric chemistry, but alongside other organic carbonyls such as formaldehyde and acetaldehyde, it is also a model system for investigating the role of intersystem crossing in photochemistry. The first absorption band is a weak broad continuum centered at 277 nm that arises from excitation of a non-bonding electron to a π* antibonding orbital, giving rise to the S_1 (^{1}n,π*) and T_1 (^{3}n,π*) states. The S_1 origin has been identified at 328.57 nm (30 435 cm^{-1}) by high-resolution laser-induced fluorescence spectroscopy.[1,2] The higher lying S_2 state has significant Rydberg character (n,3s) and has an origin at 195.2 nm (51 230 cm^{-1}). Absorption cross sections and photolysis quantum yields (as well as their pressure and temperature dependences) relevant to atmospheric chemistry are summarized in the most recent NASA/JPL evaluation.[3]

The photochemistry following excitation to the S_2 state at 193 nm has been studied extensively.[4–9] Here, we focus our discussion on the photochemistry resulting from excitation of the S_1 state. The major photolysis channel is the Norrish Type I process, in which the α-CC bond breaks to form acetyl and methyl radicals:

$$CH_3COCH_3 \rightarrow CH_3CO + CH_3 \quad 28\,920\ \text{cm}^{-1} \quad \lambda < 346\ \text{nm} \qquad \text{(I)}$$

The threshold wavelength for the observation of radical photoproducts from acetone is 305.8 nm, ascribed to the presence of a barrier on the T_1 surface that must exceeded to reach products. The radical dissociation threshold was first identified

Department of Chemistry, University of California, Irvine, Irvine, CA 92697, USA. E-mail: craig.murray@uci.edu; Tel: +1-949-824-4218

† Current address: Chemical Sciences Division, Lawrence Berkeley National Laboratory, Berkeley, California 94720, USA.

by Copeland and Crosley,[10] and is also evidenced in fluorescence measurements, which show a sharp decrease in lifetime at shorter wavelengths.[11–16] Acetyl radicals may be formed with sufficient internal energy to undergo secondary dissociation, and the triple fragmentation channel becomes increasingly important as λ is decreased.

$$CH_3COCH_3 \rightarrow CH_3 + CH_3 + CO \quad 32\,200\ cm^{-1} \quad \lambda < 311\ nm \qquad (I')$$

The photodissociation dynamics following excitation to S_1 has been investigated at 266 nm using 2 + 1 resonance-enhanced multiphoton ionization (REMPI) detection of CH_3 by Waits *et al.*[17] and at 248 nm by North *et al.* using photofragment translational spectroscopy (PTS).[8] The average translational energy release was found to be similar at both wavelengths, amounting to around 5000 cm^{-1}, indicating the role of the exit barrier in partitioning the available energy. Secondary dissociation of acetyl was significant only at 248 nm and accounted for 30% of radicals formed in the primary dissociation. Trajectory calculations by Martínez-Núñez *et al.* initiated at the T_1 barrier successfully reproduced the translational energy distributions and secondary acetyl dissociation determined from the PTS experiments.[18] Recently, Lee *et al.* have reported an ion imaging study, in which 2 + 1 REMPI was used to detect CH_3 fragments formed at several photolysis wavelengths in the range 266–312 nm.[19] Two dissociation pathways with distinct translational energy distributions were observed. Excitation at $\lambda < 306$ nm led exclusively to products with large recoil kinetic energies, consistent with dissociation over the barrier on the T_1 surface. As the photolysis wavelength was decreased, an increasing fraction of the available energy was portioned into internal degrees of freedom of the radical products. At $\lambda > 306$ nm, an additional slow component was observed in the product translational energy distribution. This new pathway to channel (I) products was well-described by a statistical model and attributed to barrierless dissociation on the S_0 surface.

Additional product channels leading to molecular products are also energetically accessible after excitation to S_1:

$$CH_3COCH_3 \rightarrow CO + C_2H_6 \quad 1450 \pm 30\ cm^{-1} \quad \lambda < 6892\ nm \qquad (II)$$

$$CH_3COCH_3 \rightarrow CH_2CO + CH_4 \quad 7310\ cm^{-1} \quad \lambda < 1368\ nm \qquad (III)$$

CO products formed at 230 nm have been found to have bimodal and *J*-dependent E_T distributions in a velocity-map ion imaging study by Goncharov *et al.*[20] The subset of slow-moving, low-*J* CO products was attributed to a roaming mechanism, while most CO products were assigned to production *via* the secondary dissociation channel (I′). To the best of our knowledge, channel (III) primary products have not been detected following excitation to S_1.

In addition to 'conventional' photochemistry experiments using nanosecond pulsed lasers, acetone has been the subject of time-resolved measurements using femtosecond pulsed lasers, typically using mass spectrometric detection techniques.[21–32] Excitation to S_2 results in direct Norrish Type I dissociation on very short (<200 fs) timescales.[21–26] The mechanistic steps following excitation to S_1 have been the subject of some debate, however, with some authors suggesting ultrafast dissociation[28,29] and others favoring a relatively long-lived excited state, with intersystem crossing to T_1 being rate limiting.[27,30–32] Despite the differing interpretations, the experimental results were in fact remarkably consistent. The long-lived excited state interpretation has been confirmed by trajectory calculations and time-resolved photoelectron spectroscopy measurements that show no signals attributable to acetyl fragments within the first 100 ps.[31,32] The ultrafast sub-picosecond signal observed in time-resolved mass spectrometry experiments was attributed to dephasing in the S_1 state as the excited molecules move out of the Franck–Condon region, and out of the non-resonant multiphoton ionization probe window. Various groups have performed *ab initio* calculations characterizing the minima, transition states, and surface crossings for acetone.[30,33–36]

In this paper, we report direct current (DC) slice imaging and photofragment excitation (PHOFEX) spectroscopy measurements exploring acetone photolysis over a broad range of wavelengths spanning the first absorption band. Methyl and acetyl radical products are formed with the available energy preferentially partitioned into translation, with the degree of internal excitation increasing at shorter photolysis wavelengths, consistent with dissociation on the T_1 surface. Time-resolved imaging measurements characterize the CH_3 radical appearance times for formation on the T_1 surface following excitation to S_1 at 284 nm and 266 nm. The onset of the secondary dissociation, or triple fragmentation, channel (I′) is identified in PHOFEX spectra obtained simultaneously probing the CH_3 and CH_3CO products. We also find a non-negligible yield of the molecular product ketene at all photolysis wavelengths. The translational energy distributions confirm that CH_2CO is formed on the singlet surface, and we tentatively suggest that a roaming mechanism may be responsible (Fig. 1).

Experimental methods

The experimental methods were identical to those used in our recent study of the near-UV photochemistry of acetaldehyde,[37] combining photofragment excitation (PHOFEX) action spectroscopy and DC slice ion imaging.[38] Both nanosecond and picosecond duration pulsed lasers were used. Briefly, a molecular beam of acetone seeded in Ar was intersected by counter-propagating photolysis and probe beams. Photofragments were detected by single-photon VUV ionization at 118.2 nm, generated by frequency tripling the 355 nm output of either a nanosecond or picosecond pulsed Nd:YAG laser in a static Xe/Ar mixture.[39] For the nanosecond experiments, a mid-band optical parametric oscillator (6 ns pulse duration, 5–7 cm^{-1} bandwidth) pumped by a Nd:YAG laser, provided tunable photolysis radiation in the range 236–308 nm. Picosecond time-resolved measurements were performed with the 266 output of the same Nd:YAG laser (28 ps pulse duration) used to generate VUV radiation; the relative time-delay was varied using a computer-controlled delay line.

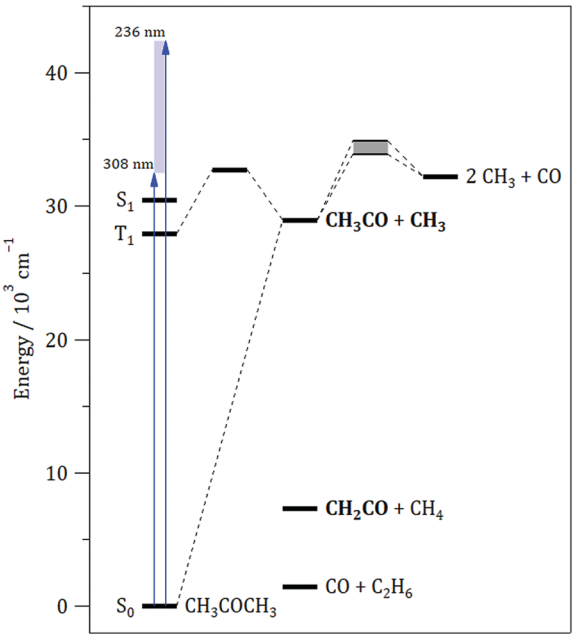

Fig. 1 Schematic energy diagram for acetone photolysis. The shaded blue area represents the range of photolysis wavelengths used (236–308 nm). Photoproducts detected by single-photon VUV ionization are emboldened.

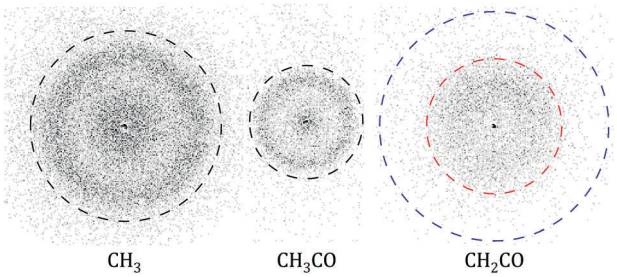

Fig. 2 Raw ion images of methyl (CH_3), acetyl (CH_3CO), and ketene (CH_2CO) fragments at a photolysis wavelength of 274 nm. Dashed circles indicate the maximum speed, v_{max}; the outer blue and inner red circles represent v_{max} for formation of singlet ketene and triplet ketene, respectively.

Results

1. DC slice ion imaging

DC sliced ion images of several acetone photofragments were recorded at photolysis wavelengths spanning the range 236–308 nm. The radical products methyl and acetyl, and the molecular product ketene have ionization potentials (IPs) of 9.84 eV, 7.0 eV, and 9.617 eV, respectively, and can be ionized at 118 nm (10.49 eV). All product species were confirmed as two-color signals in the time-of-flight mass spectrum. Acetone itself has an IP of 9.703 eV and is efficiently ionized by the VUV probe, leading to intense features in the centers of images as well as weaker off-axis multiphoton background, despite gating the detector to preferentially observe the fragment of interest in the mass spectrum. Acquisition of VUV-only images allowed this background contribution to be subtracted. As with acetaldehyde,[19,37,40] cluster formation in the supersonic expansion can be a problem. However, operating in the early part of the gas pulse and pre-cooling the sample over ice allowed the cluster contribution to the images to be minimized, albeit at the cost of reduced ion counts. Fig. 2 shows typical raw ion images of CH_3, CH_3CO, and CH_2CO obtained at a photolysis wavelength of 274 nm. The dashed circles indicate the maximum speed, v_{max}, for the detected product if all available energy is partitioned into translation. Two limits are shown on the ketene image as the photolysis wavelength provides enough energy to form either ground state singlet ketene, $^1CH_2CO$, and electronically excited triplet ketene, $^3CH_2CO$, which lies 19 060 cm^{-1} higher in energy.

Photofragment speed distributions, $P(v)$, are obtained by direct integration of the images and appropriate Jacobian transformation, and subsequently converted to total translational energy distributions, $P(E_T)$:

$$E_T = \frac{1}{2} m_A \left(1 + \frac{m_A}{m_B}\right) v_A^2$$

Here, m_A and m_B are the masses of the detected and undetected fragments, respectively. From energy conservation, the available energy, E_{AVL}, is partitioned between translation and internal excitation of the radical fragments:

$$E_{AVL} = h\nu - D_0 = E_{INT} + E_T$$

The use of non-resonant universal ionization by VUV radiation means that the E_{INT} appearing in the energy balance equation is the sum of E_{INT} for both the detected and undetected photofragments.

Channel I: CH_3 + CH_3CO. The ion images of CH_3 and CH_3CO show distinct isotropic rings corresponding to speeds close to v_{max} (2.99 km s^{-1} and 1.04 km s^{-1}, respectively, at 274 nm); the diffuse feature near the center of the image in Fig. 2 is background signal likely caused by incomplete elimination of clusters in the supersonic expansion. The ring appears in the images at photolysis wavelengths $\lambda \leq 305$ nm, consistent with the onset of dissociation over the T_1 barrier and the collapse of the S_1 fluorescence lifetime at wavelengths less than 305.8 nm.[16] As the photolysis wavelength is decreased, the ring broadens and increases in radius. The most probable speeds increasingly deviate from v_{max} at shorter wavelengths. CH_3 and CH_3CO are momentum-matched co-fragments, and consequently the total translational energy distributions, $P(E_T)$, are the same after subtraction of background signals. At all photolysis wavelengths, the E_T distributions are unimodal and well-described by a single Gaussian function. Between 304 nm and 248 nm, the average total translational energy, $\langle E_T \rangle$ increases near linearly from ~3000 cm^{-1} to ~6000 cm^{-1}, but the fraction of the available energy partitioned in to translation, $f_T = \langle E_T \rangle / E_{AVL}$, decreases from ~0.8 to 0.4. The E_T distributions broaden slightly as the available energy increases, with the energy spread, quantified by the standard deviation, σ_{E_T}, increasing from 500–2200 cm^{-1}. Using a dissociation energy of D_0 = 28 920 cm^{-1} for channel (I), the E_T distributions are transformed into E_{INT} distributions, summed over both fragments. The mean internal

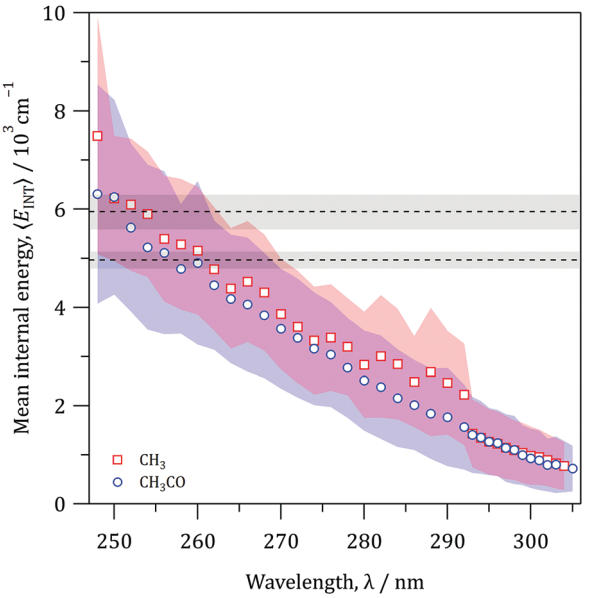

Fig. 3 Mean internal energy, $\langle E_{INT} \rangle$, derived from acetyl (blue circles) and methyl (red squares) E_{INT} distributions as a function of photolysis wavelength. The shaded areas represent the standard deviations of the distributions, σ_{E_T}, which were modelled using Gaussian functions. Dashed horizontal lines represent the barriers for secondary dissociation of CH_3CO: 5950 ± 350 cm^{-1} reported by North *et al.*[44] and 4970 ± 170 cm^{-1} reported by Tang *et al.*[45]

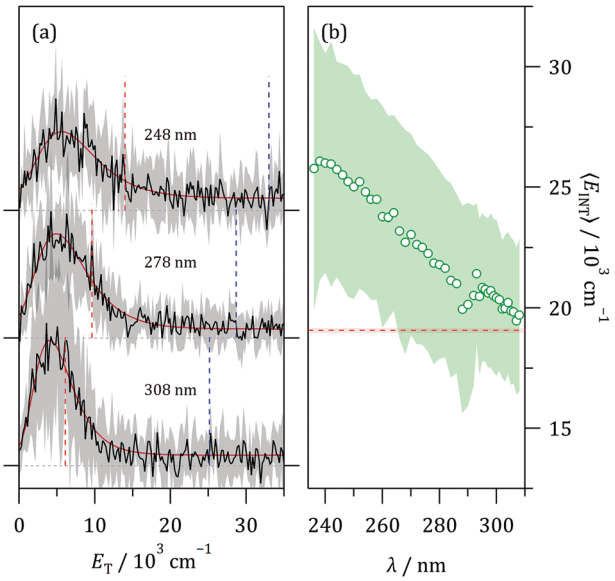

Fig. 4 (a) Total translational energy E_T distributions derived from ion images obtained probing ketene. Fits to a Gumbel distribution are shown in red. Dashed vertical lines indicate $E_{T,max}$ for formation of either singlet (blue) or triplet (red) ketene. (b) Mean internal energy, $\langle E_{INT} \rangle$, plotted as a function of photolysis wavelength. Shaded region represents the standard deviation of the E_T distributions. The horizontal dashed red line represents the threshold for formation of $^3CH_2CO$.

energy $\langle E_{INT} \rangle$, and the standard deviation of the E_{INT} distribution, $\sigma_{E_{INT}}$, are shown as a function of photolysis wavelength in Fig. 3. At longer wavelengths ($\lambda \geq 306$ nm), the excitation energy is insufficient to surmount the T_1 barrier. We also observe the statistical component characterized in detail by Lee *et al.* that is attributed to dissociation on the S_0 surface.[19]

Channel III: $CH_2CO + CH_4$. Products observed at $m/z = 42$ (CH_2CO^+) were assigned to ketene, presumably formed in conjunction with CH_4. Ion images were recorded over the range 236–308 nm, using a photolysis-ionization time delay of around 200 ns. By separating the photolysis and probe beams in time, background counts caused by the photolysis laser alone could be eliminated from the slice acquired by the detector. The images are isotropic, and show a single broad feature corresponding to production of CH_2CO fragments with speeds of ~1 km s^{-1}. Fig. 4 shows the total translational energy distributions at photolysis wavelengths of 248 nm, 278 nm and 308 nm and the variation in $\langle E_T \rangle$ and σ_{E_T} with available energy. $\langle E_T \rangle$ increases from 5450 cm^{-1} to 9290 cm^{-1} as the photolysis wavelength is decreased from 308 nm to 236 nm, while σ_{E_T} increases from 3150 cm^{-1} to 5810 cm^{-1} over the same wavelength range. The channel (III) molecular products $CH_2CO + CH_4$ lie only 7310 cm^{-1} higher in energy than the acetone parent. Values of E_{AVL} are in the range 25 200–35 100 cm^{-1}, significantly larger than those for the radical channel (I). The fraction of E_{AVL} partitioned into translation is independent of photolysis wavelength, and has an average value of 0.23 ± 0.01. The remainder must be partitioned into internal degrees of freedom of the CH_2CO and CH_4 products, which, in addition to rotation and vibration, can also include electronic excitation, as the lowest triplet state of ketene, $^3CH_2CO$, is accessible.

$$CH_3COCH_3 \rightarrow {}^3CH_2CO + CH_4 \quad D_0 = 26\,370 \pm 100\ cm^{-1} \quad \lambda < 379\ nm \qquad (III')$$

We note that the CH_2CO ion image at 274 nm shown in Fig. 2 appears at first glance to extend only as far as v_{max} determined using the thermodynamic threshold for $^3CH_2CO$ formation. However, the E_T distributions, particularly at longer photolysis wavelengths, show that a significant fraction of the products are formed with $E_T > E_{T,max}$ for the triplet channel. The 308 nm data shown in Fig. 4 serve as an example. Around half the E_T distribution extends beyond the triplet limit and while in general $\langle E_{INT} \rangle$ is greater than the energy required to form triplet products at all photolysis wavelengths, the spread in $P(E_T)$ represented by $\sigma_{E_{INT}}$ means that a significant fraction of the products have internal energies that are below the triplet threshold. Again, we note that E_{INT} here represents the sum of the internal energies of the CH_2CO and the CH_4 fragments.

2. Time-resolved ion imaging

CH_3 radical appearance times were measured by recording ion images as a function of the photolysis-ionization time delay, Δt. Measurements using the nanosecond pulsed lasers were made over a 200 ns range at photolysis wavelengths of 254 nm, 264 nm, 274 nm, and 284 nm. Only 284 nm photolysis led to a series of ion images that showed a time dependence; at the shorter wavelengths, CH_3 production appears to be prompt on the timescale of the laser pulses. The photolysis pulse alone

produced background m/z = 43 (CH_3CO^+) ion signal, that overwhelmed the two-color signal and precluded any time-resolved measurements detecting the acetyl radical.

Fig. 5 shows a subset of the CH_3 speed distributions derived from a series of ion images recorded as Δt was varied over 200 ns at a photolysis wavelength of 284 nm. The bottom trace in Fig. 5(a) was obtained with reversal of the time ordering of the laser pulses and represents a broad background signal that extends far beyond v_{max} of 2700 m s^{-1} and is presumably caused by multiphoton processes. The expected T_1 component appears strongly at early times and increases in magnitude at longer delays. The shape of the distribution, which is characterized by a Gaussian function with average speed $\langle v \rangle$ and standard deviation σ_v is independent of time delay; the average over the delays results in $\langle\langle v \rangle\rangle$ = 2230 ± 10 m s^{-1} and $\langle \sigma_v \rangle$ = 360 ± 20 m s^{-1}. Fig. 5(b) shows the speed distributions for T_1 products after subtraction of the background contribution. Aside from the increase in the magnitude, the speed distribution is otherwise unchanged over the range of delays; the average speeds, standard deviations, and the relative area of the T_1 component at each delay are shown in Fig. 6. Fitting the time dependence of the T_1 signal to an exponential rise

$$S(t) = A\left[1 - \exp\left(\frac{t - t_0}{\tau}\right)\right]$$

yields a time constant of τ = 42 ± 9 ns. We note that the fit does not pass through the origin, instead returning t_0 = −21 ± 7 ns. This offset is much greater than the 6 ns laser pulse duration or the uncertainty in the delay time, which is controlled electronically and monitored with a fast photodiode. Constraining the value of t_0 to be zero results in fit that is significantly poorer, with τ = 19 ± 3 ns. It is clear from Fig. 5 that the T_1 component is absent at $\Delta t < 0$ but is significant even at the shortest delay of Δt = +10 ns, accounting for around half the maximum signal observed.

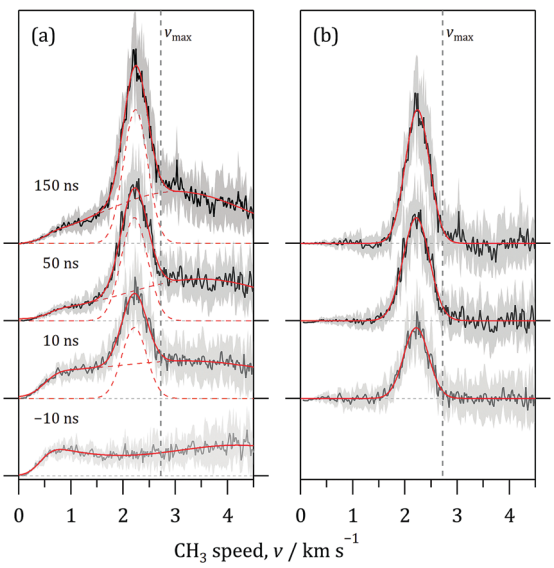

Fig. 5 Time-resolved CH_3 speed distributions measured using nanosecond pulsed lasers at a photolysis wavelength of 284 nm: (a) raw speed distributions, (b) after subtraction of background signals. Red curves are fits to the experimental data. Dashed vertical lines indicate v_{max}.

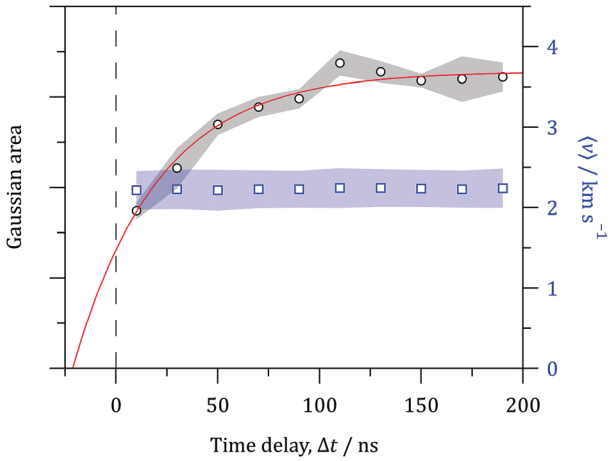

Fig. 6 Left axis: CH_3 product appearance kinetics measured using nanosecond pulsed lasers at 284 nm (black circles). The red curve is the fit to a single exponential rise (red line). Right axis: The mean speed, $\langle v \rangle$, at each delay (blue squares). The blue shaded area represents the standard deviation of the speed distribution, σ_v.

Picosecond time-resolved measurements were performed at a fixed photolysis wavelength of 266 nm, again detecting products by single-photon VUV ionization at 118 nm. The time delay between the laser pulses Δt could be varied between −1000 ps and +2500 ps using a computer-controlled delay line; once again, $\Delta t > 0$ corresponds to the 266 nm pulse preceding the 118 nm pulse. As in our previous work on acetaldehyde,[37] the 118 nm ionization pulse readily ionizes the parent molecule and reversing the time ordering of the laser pulses results in 266 nm photodissociation of the $CH_3COCH_3^+$ cation, directly producing ionic fragments. Fig. 7 shows the variation of the total m/z = 15 (CH_3^+) ion signal obtained from transient mass spectra, recorded with electrodes configured for conventional Wiley–McLaren mass spectrometry. The CH_3^+ ion signal increases as Δt becomes both increasingly positive and negative. For $\Delta t < 0$, the signal increases within the cross-correlation time of the laser pulses, and then remains constant. In contrast, the CH_3^+ signal increases more gradually for $\Delta t > 0$.

The rising edge at $\Delta t < 0$ is instrument-limited. The convolution of a Gaussian and Heaviside step function is used to describe this signal:

$$S(t) = \frac{A}{2}\left[1 + \mathrm{erf}\left(\frac{t_0 - t}{\sqrt{2}\sigma}\right)\right]$$

Here, t_0 is the zero of time at which both photolysis and probe lasers are overlapped and σ is the Gaussian width representing the cross-correlation time. The value of σ was determined by fitting transients for a dissociation known to be prompt ($CH_2I_2 \rightarrow CH_2I + I$) and was constrained during subsequent fitting. The value of σ = 22 ps implies an instrument time resolution of 37 ps. The slowly rising edge is modelled as the convolution of a Gaussian function with the product of a

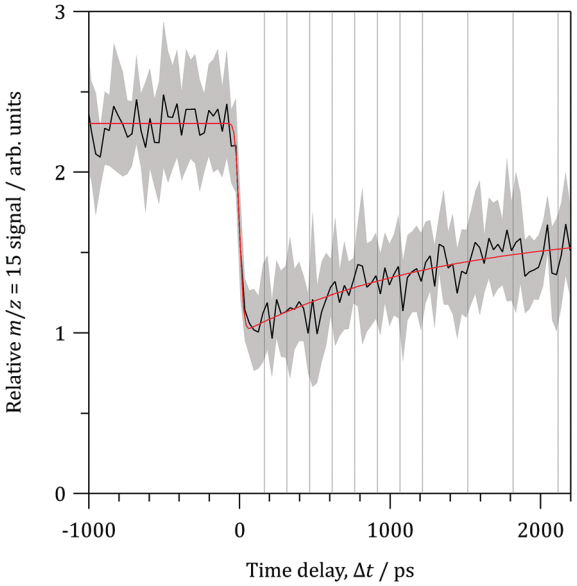

Fig. 7 Transient m/z = 15 (CH_3^+) ion signal plotted as a function of time delay, Δt, between 28 ps duration 266 nm and 118 nm pulses. $\Delta t < 0$ corresponds to the 118 nm pulse preceding the 266 nm pulse; the signal arises from dissociation of the parent cation. $\Delta t > 0$ corresponds the 266 nm pulse preceding the 118 nm pulse; the signal arises from VUV ionization of CH_3 photofragments. A time-independent background signal also contributes. The red curve is a fit to the experimental data, as described in the text. The time constant for the increasing signal at $\Delta t > 0$ is 1350 ± 530 ps. Vertical lines indicate delays at which ion images were recorded.

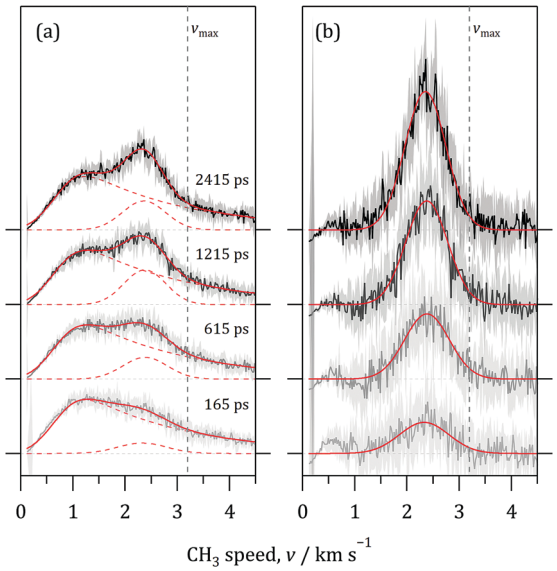

Fig. 8 CH_3 speed distributions at selected photolysis-ionization time delays, Δt, as indicated, at a photolysis wavelength of 266 nm. (a) Complete bimodal speed distributions, which comprise a broad, slow, and time-independent contribution and a narrow, fast, and time-dependent component. (b) Time-dependent component after subtraction of the slow component. Solid red curves are fits to the experimental data and dashed curves indicate the individual components. The dashed vertical lines indicate v_{max} of 3.2 km s^{-1}.

Heaviside function and a single exponential rise with time constant τ:

$$S(t) = \frac{A}{2}\left\{1 + \mathrm{erf}\left(\frac{t-t_0}{\sqrt{2}\sigma}\right) - \exp\left(\frac{\sigma^2 - 2(t-t_0)\tau}{2\tau^2}\right) \times \left[1 + \mathrm{erf}\left(\frac{(t-t_0)\tau - \sigma^2}{\sqrt{2}\sigma\tau}\right)\right]\right\}$$

The transient ionization data in Fig. 7 was fit to a sum of these two functions, which describe the time evolution of the m/z = 15 signal at positive and negative Δt, respectively. The CH_3 appearance time constant is determined to be τ = 1350 ± 530 ps.

Ion images of CH_3^+ were recorded at twelve different delays between +115 ps and +2415 ps, as indicated in Fig. 7. The speed distributions are bimodal at all time delays, as shown in Fig. 8. A broad, time-independent component peaks near 1.2 km s^{-1}, and extends beyond the maximum speed of 3.2 km s^{-1}, again suggesting a multiphoton process is responsible. Superimposed is a time-dependent, translationally fast component peaking near 2.4 km s^{-1} and with a FWHM of 1.0 km s^{-1} that is the same as the speed distribution obtained in the nanosecond measurements and can be attributed to dissociation on the T_1 surface. The speed distributions were fit to an exponentially-modified Gaussian function and a Gaussian function to separate the overlapping contributions. The fast Gaussian component comprises around 7% of the total speed distribution at Δt = +115 ps, increasing to 23% at Δt = +2415 ps, which is consistent (within error) with the modest increase in the m/z = 15 signal observed in the transient mass spectra. The time evolution of the fast component of the speed distribution following subtraction of the time-independent background signal is shown in Fig. 8. The mean speed and standard deviation of the fast-moving T_1 component does not change with delay time: across all delays $\langle\langle v\rangle\rangle$ = 2360 ± 20 m s^{-1} and $\langle\sigma_v\rangle$ = 570 ± 40 m s^{-1}. The area of the T_1 component, shown as a function of delay time in Fig. 9, is fit to a single exponential rise, returning a time constant of 1490 ± 140 ps, which agrees with the rise time obtained from the transient ionization data. The fit returns t_0 = −210 ± 30 ps, which again is greater than would be expected from the instrument function or uncertainties in the delay time. In this case, however, the apparent non-zero value of t_0 could also arise from incomplete subtraction of the multiphoton background signal, which is far larger than the time-resolved component. Constraining the fit by setting t_0 = 0, yields a smaller time constant of 680 ± 120 ps and a poorer fit to the experimental data.

3. Photofragment excitation action spectroscopy

PHOFEX action spectra of CH_3COCH_3 were recorded over the wavelength range 235–291 nm. The spectra corresponding to detection of CH_3, CH_3CO and CH_2CO fragments were extracted from the corresponding ion signals in wavelength-dependent time-of-flight mass spectra. The photolysis-ionization time delay was around 200 ns. The relatively long delay ensures that the PHOFEX spectra measure the asymptotic yield of each fragments, at least for $\lambda \leq$ 284 nm where appearance times

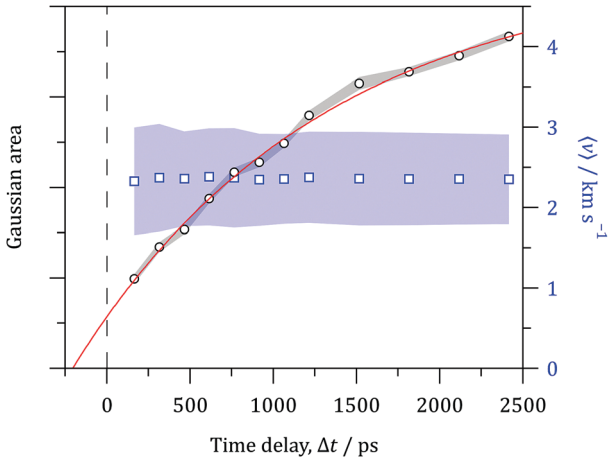

Fig. 9 Left axis: Areas of the Gaussian components of the CH_3 speed distributions plotted against photolysis-ionization time delay, Δt. The red curve is a fit of the experimental data to a single exponential rise with time constant is 1490 ± 140 ps. Right axis: Mean speeds $\langle v \rangle$ (blue squares) and standard deviations, σ_v (blue shaded area).

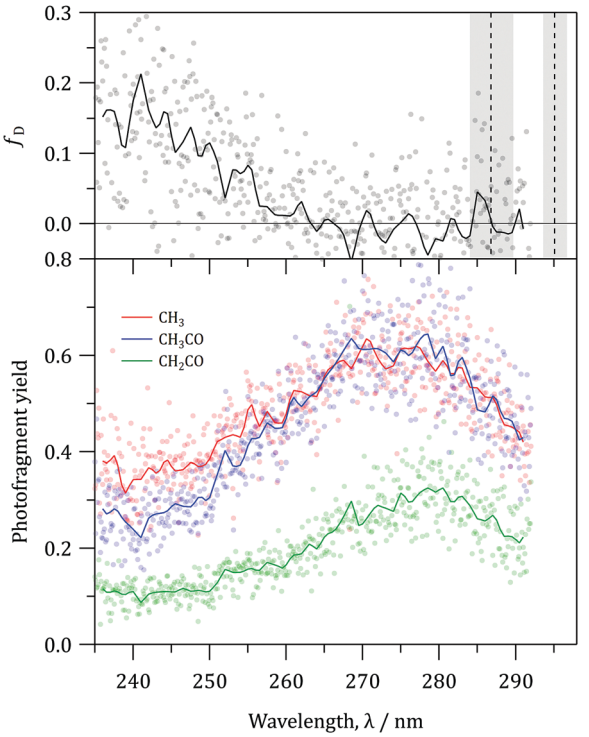

Fig. 10 Bottom panel: Photofragment excitation spectra of acetone probing methyl (red), acetyl (blue), and ketene (green). The relative photofragment yields were corrected for the respective photoionization cross sections, as described in text, and subsequently scaled to match the channel (I) yield of ~0.6 at 280 nm.[3] Top panel: Estimated fraction of acetyl primary products that subsequently dissociate to CH_3 + CO. Dashed vertical lines and shaded areas show thresholds (and uncertainties) for the reported values of the acetyl dissociation barrier.[44,45]

are short. The lower panel of Fig. 10 shows the PHOFEX spectra, which have been corrected for variation in the photolysis laser fluence across the wavelength region covered and the relative detection sensitivities of the photofragments (discussed below). The spectra broadly follow the shape of the absorption band for all fragments. Unsurprisingly, probing the CH_3 and CH_3CO radicals results in nearly identical spectra, with maximum yields obtained at 274 nm. The ratio of the raw CH_3CO and CH_3 signals is constant at $\lambda > 260$ nm; over the wavelength range 281–291 nm, the average ratio is 1.71 ± 0.07, indicating a greater detection sensitivity for acetyl than for methyl at 118 nm, assuming the ionization efficiency is independent of the vibrational state. The photoionization cross section of CH_3 at 118 nm has been reported to be 6.7 Mb,[41] implying that that of CH_3CO is ~11.4 Mb. The relative ease with which acetyl can be detected using 118 nm ionization confirms our earlier assertion that the CH_3CO + H channel of acetaldehyde is minor, as expected.[37] The spectrum obtained detecting CH_2CO is qualitatively similar, although the maximum yield is observed at a slightly longer wavelength of 278 nm. Ketene has a reported photoionization cross section at 118 nm of 24.8 Mb,[42] almost four times that of CH_3, and appears to be formed with significant yield.

After correcting for the relative detection sensitivities of CH_3 and CH_3CO, the action spectra in Fig. 10 can be seen to diverge at $\lambda < 260$ nm, where production of an excess of CH_3 over CH_3CO is observed. As the product pair for channel (I), one would expect the relative yields of both to remain constant:

$$Y_{CH_3} = Y_{CH_3CO} = \sigma\Phi_I$$

Here Φ_I is the primary photolysis quantum yield for channel (I) and σ is the absorption cross section – both are wavelength-dependent. However, secondary dissociation of internally excited acetyl radicals leads to an increase in the relative yield of CH_3 and corresponding reduction in that of CH_3CO.

$$CH_3COCH_3 + h\nu \rightarrow CH_3 + CH_3CO^* \rightarrow CH_3 + CH_3 + CO \quad I \rightarrow I'$$

Including secondary dissociation, the yields of CH_3 and CH_3CO can be written as

$$Y_{CH_3} = \sigma\Phi_I(1 + f_D)\ Y_{CH_3CO} = \sigma\Phi_I(1 - f_D)$$

where f_D is the fraction of CH_3CO that dissociates, which in turn leads to

$$f_D = \frac{Y_{CH_3} - Y_{CH_3CO}}{Y_{CH_3} + Y_{CH_3CO}}$$

The relative yields of CH_3 and CH_3CO are determined directly from the scaled PHOFEX spectra. The upper panel of Fig. 10 shows the fraction of internally excited CH_3CO radicals that dissociate as a function of photolysis wavelength. The fraction dissociated remains at zero until $\lambda < 260$ nm, beyond which it increases steadily, reaching values of around 0.2 at the shortest photolysis wavelengths.

Discussion

1. Radical channel: CH_3 + CH_3CO

Fast moving methyl and acetyl fragments are detected at photolysis wavelengths $\lambda < 306$ nm, which is consistent with the observed shortening of the S_1 fluorescence lifetime and the

opening of the triplet dissociation channel.[10,12–16,19] The E_T distributions are narrow and peak near $E_{T,max}$ at wavelengths corresponding to excitation close to the T_1 barrier. As the available energy is increased, the distributions broaden and the peaks deviate ever more from $E_{T,max}$, indicating a decreasing fraction of the available energy is partitioned into translation. Across the range 248–304 nm, E_{AVL} for dissociation to the radical products spans 4000–11 400 cm^{-1}. The mean translational energy, $\langle E_T \rangle$ increases linearly from 3000–5000 cm^{-1} and the standard deviation σ_{E_T} increases from 500–2200 cm^{-1}. Similar values are obtained probing either CH_3 or CH_3CO. The mean translational energies are in moderately good agreement with previous measurements. Waits *et al.* measured a value of 3830 cm^{-1} for E_T following photolysis at 266 nm, which is slightly lower than our value of 4620 cm^{-1}. Better agreement is obtained with North *et al.* who reported $\langle E_T \rangle$ = 4970 cm^{-1} and σ_{E_T} = 1800 cm^{-1} at 248 nm, while our equivalent values are 5100 and 2200 cm^{-1}, respectively.[8,17] In a recent ion imaging study, Lee *et al.*[19] measured $\langle E_T \rangle$ values 3510–5430 cm^{-1} in the photolysis wavelength range 304–266 nm, finding a linear relationship between $\langle E_T \rangle$ and E_{AVL}. In the same wavelength range, we find marginally lower values of $\langle E_T \rangle$ of 3260–4620 cm^{-1} while the linearity is maintained across the greater range of E_{AVL}, albeit with a slightly gentler slope (0.25 rather than 0.33). The lower values of $\langle E_T \rangle$ in the current work compared to those measured by Lee *et al.* can be rationalized by the different ionization schemes used. The REMPI scheme used by Lee *et al.* selectively detects comparatively low-*J* levels of the vibrational ground state CH_3, while VUV ionization detection of CH_3 or CH_3CO is universal, leading to contributions from internally excited radical fragments with lower recoil velocities. This effect is also evident in the slightly broader rings in the images when using VUV ionization. The radical E_T distributions shows the same photolysis wavelength dependence as observed for acetaldehyde,[37] with f_T values of approximately 0.8 near threshold decreasing to around 0.5 at $E_{AVL} \approx 8000$ cm^{-1}. The trends are consistent with earlier measurements and the conclusion that dissociation occurs over the T_1 barrier following intersystem crossing.[8,17,19] The change in the shapes of the E_T distributions can be explained by a mixed impulsive/statistical model in which the reverse barrier height largely dictates E_T and the remainder of E_{AVL} is distributed statistically among the internal degrees of freedom of the radical products.[19,43]

The T_1 mechanism leading to radical products shows many similarities to that of acetaldehyde but there are two significant differences. First, we see no evidence of an additional pathway at shorter photolysis wavelengths that results from dissociation on S_0 accessed *via* an S_1/S_0 conical intersection, and second, we do see evidence of triple fragmentation in the PHOFEX spectra. Lee *et al.* reached a similar conclusion regarding the absence of an S_0 channel at shorter wavelengths, although their measurements extended only as far as 266 nm.[19] *Ab initio* calculations have placed the S_1 barrier that must be overcome to reach the conical intersection at 38 000–46 700 cm^{-1}, which implies a threshold wavelength range of 263–214 nm.[30,34–36] The lack of any clearly observable signal attributable to the conical intersection channel suggests that the barrier lies to the higher energy end of the range predicted by theory. Measurements seeking to identify this pathway at higher energies will, however, be complicated by triple fragmentation. The methyl radical quantum yield approaches two at shorter photolysis wavelengths because of secondary dissociation of internally excited acetyl radicals [channel (I′)]. Previously, North *et al.* estimated the fraction of acetyl photofragments that dissociate at 248 nm to be $f_D = 0.30$.[8] Accessing the triple fragmentation products requires a photon energy of at least 32 200 cm^{-1}, which corresponds to a threshold wavelength of 311 nm. However, the barrier to acetyl dissociation pushes the threshold to shorter wavelengths. Values of 4970 ± 180 cm^{-1} and 5950 ± 350 cm^{-1} have been reported for the acetyl exit channel barrier, implying threshold wavelengths of 295 nm or 286 nm.[44,45]

The PHOFEX spectra in Fig. 10 suggest that the threshold for channel (I′) is closer to 260 nm, or ~9500 cm^{-1} above D_0 for channel (I). Secondary dissociation is only possible for the subset of acetyl radicals formed with E_{INT} greater than the barrier, which is determined by the dynamics of the primary dissociation process. Acetyl radicals are primarily formed on the T_1 surface, which partitions most of the available energy into translation. In the threshold wavelength range 286–295 nm, values of $\langle E_{INT} \rangle$ are 1300–2000 cm^{-1}, and the distributions are characterized by σ_{E_T} of 700–1000 cm^{-1}. That is, at best, only the subset of acetyl radicals with E_{INT} more than three standard deviations from the mean have enough energy to dissociate, assuming the lower barrier; at best, because E_{INT} also contains an unquantified contribution from the methyl partner. Consideration of only threshold energies or wavelengths is unlikely to be predictive for the onset of secondary dissociation, without first understanding the energy partitioning of the primary dissociation process. The upper panel of Fig. 10 suggests $f_D \approx \sim 0.12$ at 248 nm, which is smaller than the value of 0.30 determined by photofragment translational spectroscopy by North *et al.*[8] The apparent discrepancy could arise from the time required for acetyl to undergo unimolecular dissociation, although RRKM calculations suggest sub-nanosecond lifetimes for acetyl with internal energy only slightly above the barrier.

Returning to the primary dissociation of the parent acetone, time-resolved measurements at 284 nm and 266 nm find appearance time constants for CH_3 of 42 ± 7 ns and 1490 ± 140 ps, respectively. In contrast to acetaldehyde,[37] the time-dependent CH_3 speed distributions are unimodal and, in all regards, bear the hallmark of dissociation occurring exclusively on the T_1 surface. In the conventional view of carbonyl photochemistry, the rate limiting step for product formation is either $S_1 \rightarrow T_1$ intersystem crossing, $k_{ISC}^{S_1 \rightarrow T_1}$, or the subsequent dissociation on the T_1 surface, $k_D^{T_1}$. Excitation at 284 nm and 266 nm prepares the S_1 state with energies 2500 cm^{-1} and 4900 cm^{-1} above the T_1 barrier. RRKM calculations by Sakurai and Kato find values of $k_D^{T_1}$ in the range 10^{11}–10^{12} s^{-1} and consequently T_1 lifetimes of only 1–10 ps.[33] Dissociation once on the T_1 surface is fast relative to the rate of intersystem crossing.

The CH_3 appearance time constant at 266 nm is in excellent agreement with the fluorescence lifetime of <1.6 ns at 260 nm,[11]

implying that the loss of population from S_1 is dominated by $k_{ISC}^{S_1 \rightarrow T_1}$. Subsequent dissociation on the T_1 surface happens on a shorter timescale, as indicated by the results of the RRKM calculations. The rate of intersystem crossing in acetone of $k_{ISC}^{S_1 \rightarrow T_1} = 0.67 \pm 0.06\ ns^{-1}$ appears, therefore, to be around six times slower than in acetaldehyde, where the CH_3 appearance time constant of 240 ps was attributed to a rate of $k_{ISC}^{S_1 \rightarrow T_1} = 4.2\ ns^{-1}$ at 266 nm. The difference in intersystem crossing rates is surprising, as the spin–orbit coupling constants are similar and the T_1 density of states is significantly greater in the larger molecule. Computational work by Maeda *et al.* has addressed the issue of slow intersystem crossing in acetone,[35] showing that there is no explicit crossing between the S_1 and T_1 states near the Franck–Condon region and that the minimum energy crossing occurs at relatively high energy.

The picosecond time-resolved imaging measurements at 266 nm suggest a small non-zero signal at t_0, that could be indicative of (minor) product formation on a still faster timescale. The dynamics following excitation to S_1 has been the subject of several femtosecond time-resolved measurements using mass spectrometry, ion imaging and photoelectron spectroscopy.[27–32] While the experimental observations were in good agreement, substantially different interpretations were offered, with some authors proposing direct impulsive dissociation and others arguing for a long-lived excited state. The CH_3 speed distributions are characteristic of dissociation over a barrier, with the T_1 state being the most likely candidate. While the change in the magnitude of the T_1 component with increasing delay is clear, we are reluctant to conclude that there is a sub-ps component based on the current experimental data. As such, the results are consistent with the ultrafast study of Rusteika *et al.*, who concluded that all α-CC fission occurs on a timescale greater than 100 ps.[31] At the shortest nominal time delay of 165 ps, the magnitude of the T_1 component is small and could be affected by inadequate subtraction of the time-independent background or uncertainty in the absolute time delay.

At 284 nm, the T_1 products appear to be formed on two distinct timescales. As noted above, RRKM calculations suggest a T_1 lifetime of only ~10 ps at 284 nm and dissociation once on T_1 is effectively prompt on the nanosecond timescale of the measurements. However, unlike at 266 nm where the CH_3 formation time constant is comparable to the <1.6 ns fluorescence lifetime, the 42 ns appearance time constant at 284 nm is significantly longer than the comparably short fluorescence lifetimes of 1.7 ns and 2.9 ns measured at 270 nm and 295 nm, respectively.[11] The unquantified <10 ns component is, however, consistent with the observed fluorescence lifetimes. If the slow formation rate of 0.024 ns^{-1} were due to $k_{ISC}^{S_1 \rightarrow T_1}$, another significantly faster non-radiative process, presumably $S_1 \rightarrow S_0$ internal conversion, must be active to remove population from S_1 otherwise fluorescence would be observed. Calculations by Favero *et al.* have suggested that $S_1 \rightarrow S_0$ internal conversion may be competitive with $S_1 \rightarrow T_1$ intersystem crossing,[36] with similar rate constants for both processes ($k_{IC}^{S_1 \rightarrow S_0} = 4.8\ ns^{-1}$ and $k_{ISC}^{S_1 \rightarrow T_1} = 3.5\ ns^{-1}$) and an overall S_1 lifetime of around 2 ns that is consistent with the experimentally observed fluorescence lifetime. The ps time-resolved time-of-flight spectra obtained also provide some experimental evidence to support competitive internal conversion at 266 nm. The parent ion signal increases in magnitude for $\Delta t > 0$ with a time constant of 3.7 ± 2.1 ns, suggesting population transfer to a state that is ionized with greater efficiency with a rate of 0.27 ± 0.15 ns^{-1}. Internal conversion to form hot S_0 is more likely than T_1, since the latter should dissociate on a ~1 ps timescale.

An intersystem crossing rate of $k_{ISC}^{S_1 \rightarrow T_1} \approx 0.3\ ns^{-1}$ would be fast enough to account for the significant T_1 component observed in the CH_3 speed distributions at short delays, which has reached half its maximum by Δt = +10 ns. At longer time delays, the CH_3 speed distributions remain characteristic of dissociation on T_1, as shown in Fig. 5, with no time-dependent evolution of either $\langle v \rangle$ or σ_v. The slow increase in the CH_3 signal could be explained by a two-step mechanism in which population is first transferred from $S_1 \rightarrow S_0$ with rate $k_{IC}^{S_1 \rightarrow S_0}$ and subsequently from $S_0 \rightarrow T_1$ with rate $k_{ISC}^{S_0 \rightarrow T_1}$. Rapid dissociation on the T_1 surface follows. If depopulation of S_1 *via* $k_{IC}^{S_1 \rightarrow S_0}$ is indeed comparable to $k_{ISC}^{S_1 \rightarrow T_1}$, the observed slow appearance time constant would be attributable to the rate of $S_0 \rightarrow T_1$ intersystem crossing. The proposed sequential $S_1 \rightarrow S_0 \rightarrow T_1$ mechanism for slow formation of radical products on T_1 at 284 nm relies on the viability of the S_0 state to act as a temporary population reservoir, with a surprisingly long lifetime on the order of several tens of nanoseconds. Unimolecular dissociation on S_0 to $CH_3 + CH_3CO$ would lead to a statistical component in the E_T distribution, analogous to that observed at $\lambda > 306$ nm where the T_1 mechanism is inaccessible, but is not observed.[19] Once on the S_0 surface, several other pathways are likely to be competitive with the proposed intersystem crossing to the T_1 surface. Isomerization to propen-2-ol is also accessible, although the constancy of the speed distributions as a function of delay time suggest that the slow onset is unlikely to be due to dissociation of this species. Dissociation channels on S_0 that lead to molecular products such as ketene, as will be discussed below, would also be open. We note that CH_2CO^+ is not observed in the picosecond time-dependent mass spectra at 266 nm, which is consistent with hot S_0 produced *via* internal conversion having a relatively long lifetime. Variational transition state theory calculations to characterize the lifetime of hot S_0 would be helpful.

An alternative interpretation for the time dependence following photolysis at 284 nm is that the <10 ns component results from fast $S_1 \rightarrow T_1$ intersystem crossing, but the slower growth is due to another process, such as secondary dissociation of hot CH_3CO. For this to be the case, the E_T distribution would have to be indistinguishable from that which results from dissociation on T_1. Unimolecular decomposition of CH_3CO also occurs over a barrier, although the reverse barrier height of 1680–2660 cm^{-1} is smaller than that on the acetone T_1 surface of 3670 cm^{-1}.[44,45] Consequently, the E_T distributions resulting from hot CH_3CO dissociation would be broader and peak at lower average E_T than those observed for dissociation of the parent molecule on T_1,

and a time-dependent evolution of the shape would be expected. Furthermore, secondary dissociation of hot CH_3CO would lead to an enhancement of CH_3 over CH_3CO, an effect that is not observed in the PHOFEX spectra until $\lambda < 260$ nm.

2. Molecular channel: $CH_2CO + CH_4$

To the best of our knowledge, the molecular channel (III) has not been identified previously after photolysis of acetone in the first absorption band, although it has been suggested as a minor channel that accounts for ≤ 0.02 of the overall photolysis yield at 193 nm.[5] North *et al.* noted that no signal attributable to CH_4 or CH_2CO was observed in their PTS experiments at 193 nm, but did not comment explicitly comment on this channel at 248 nm.[8] The absolute photoionization cross sections for methyl and ketene near 118 nm and the channel (I) quantum yield at $\lambda > 279$ nm are known, allowing the yield of channel (III) to be estimated. The PHOFEX spectra shown in Fig. 10 have been scaled such that that $\Phi_I = 0.6$ at 280 nm, consistent with previous measurements.[3] The quantum yield of channel (III) products is not insignificant; it approaches half that of channel (I) across the first absorption band, and reaching a surprisingly large maximum value of $\Phi_{III} \approx 0.3$ at 278 nm. The estimated ketene quantum yield relies on the assumption that internal excitation does not significantly affect the photoionization cross section and consequently the detection sensitivity. The translational energy distributions shown in Fig. 4 indicate that the molecular products are formed with significant internal excitation, which may enhance the photoionization cross section. A more reliable determination of the ketene quantum yield will require better characterization of the detection sensitivity dependence on the degree of internal excitation.

Although $^3CH_2CO$ is energetically accessible at the photolysis wavelengths used (the threshold is <379 nm), we rule it out as a possible product. First the E_T distributions, particularly at longer photolysis wavelengths (see Fig. 4), extend far beyond the reduced value of $E_{T,max}$ that would result from electronic excitation of ketene. Secondly, although $\langle E_{INT} \rangle$ is larger than the energy required to form $^3CH_2CO$, the spread in the distribution characterized by σ_{E_T} means that the distributions extend significantly below the triplet origin. This effect is compounded when one recalls that the E_{INT} distributions are sums over both the detected and undetected fragments. Any internal excitation of the CH_4 co-fragment would reduce $E_{INT}(CH_2CO)$ even further below the triplet energy. Secondary dissociation of acetyl radicals to form $CH_2CO + H$ can also be ruled out on energetic grounds. Loss of a hydrogen atom from acetyl requires $E_{INT} > 14\,700$ cm^{-1}, placing the threshold wavelength near 229 nm. At the shortest photolysis wavelength of 236 nm, the value of $\langle E_{INT} \rangle$ for both CH_3 and CH_3CO of around 10 000 cm^{-1} falls short of the energy required. We conclude that CH_2CO is formed in its singlet ground state, and is not a product of a secondary dissociation.

Dissociation to form molecular products in organic carbonyls can occur on the S_0 surface following internal conversion; such pathways are well known in formaldehyde and acetaldehyde, and proceed *via* tight transition states at energies near the onset of the radical channels.[46] Infrared multiphoton dissociation (IRMPD) of acetone under collision-free conditions showed no evidence of ketene formation.[47] Ketene has been identified as a major product of acetone pyrolysis under collisional conditions, likely due to secondary reactions.[48] The absence of ketene in the collision-free IRMPD experiments suggests that the barrier to dissociation on S_0 is significantly higher than the 28 920 cm^{-1} threshold for breaking a C–C bond to form radical products while the observation of CH_2CO at 308 nm suggests an upper limit of 32 470 cm^{-1}. The product energy partitioning, however, argue against dissociation *via* a conventional transition state on S_0. As clearly demonstrated by the radical product formation on the T_1 surface, dissociation over a barrier effectively partitions E_{AVL} into translation ($f_T \approx 0.8$ for methyl and acetyl near the T_1 barrier). Yet for ketene, $\langle E_T \rangle$ values in the range 5500–9300 cm^{-1} mean that $f_T \approx 0.2$, which is too small for dissociation over a high barrier. Alternatively, the modest values of $\langle E_T \rangle$ could instead be interpreted as indicating a reverse barrier of a similar height; that is, it would imply a barrier on S_0 for dissociation to molecular products of around 13 000 cm^{-1}, significantly lower than the C–C bond dissociation energy. The failure then to observe CH_2CO as a product in the IRMPD work would be even more surprising, as this pathway would be by far the lowest energy route to dissociation in acetone.

The supposed existence of high barriers on S_0 for dissociation of acetone to form $CH_2CO + CH_4$ is confirmed by *ab initio* calculations characterizing the transition state.[49] We have also identified an analogous transition state for unimolecular dissociation from the tautomer propen-2-ol. Attempts to identify equivalent transition states on the T_1 surface were unsuccessful. Kable and co-workers have presented evidence for phototautomerization to form vinyl alcohol from acetaldehyde following excitation in the near-UV and internal conversion to S_0.[50,51] The equivalent tautomerization of acetone to form propen-2-ol on S_0 has been calculated to have a barrier of 24 820 cm^{-1},[35] and consequently is accessible at all excitation wavelengths. Optimized geometries of the transition states for dissociation of acetone and propen-2-ol have been calculated at the MP2/def2-SVP level of theory using the MOLPRO 2012.1 quantum chemistry package,[49] while intrinsic reaction coordinate calculations, shown in Fig. 11, confirm that the transition states connect the expected reactants and product species. Relative to the channel (III) products, the reverse barrier heights are large and comparable: 24 000 cm^{-1} for acetone and 29 000 cm^{-1} for propen-2-ol. Dissociation of either tautomer *via* either of these conventional transition states on S_0 would partition a large fraction of the available energy into translation, a signature that is absent from the experimental data. At this level of theory, the threshold wavelength for the molecular dissociation channel in propen-2-ol is predicted to be around 267 nm.

A second mechanism known to lead to molecular products in the photochemistry of organic carbonyls is roaming.[52–55] Roaming in formaldehyde (or acetaldehyde) results in the formation of and highly internally excited H_2 (or CH_4), in conjunction with low-J CO, contrasting with the conventional S_0 transition state mechanism, which results in high-J CO and

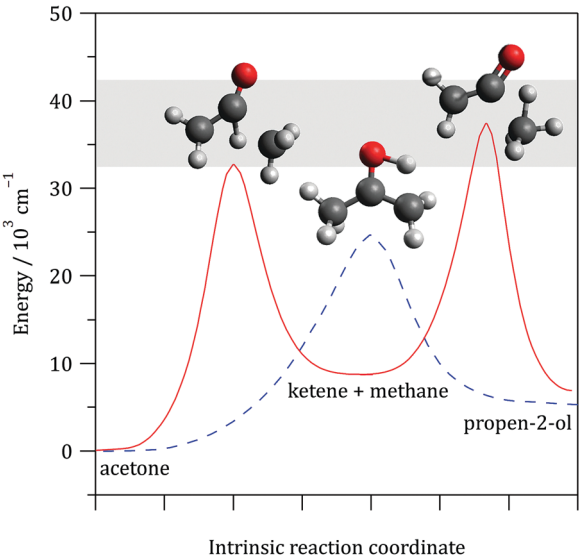

Fig. 11 Intrinsic reaction coordinates calculated at the MP2/def2-SVP level for keto–enol tautomerization (blue dashed) and dissociation of acetone and propen-2-ol to form ketene + methane (red solid). Transition state geometries are shown. The shaded gray area represents the range of excitation energies used in the experiments.

significant translational energy release.[56–58] Goncharov *et al.* have identified signatures consistent with an analogous roaming mechanism in the photochemistry of acetone, finding *J*-dependent bimodal CO E_T distributions at 230 nm.[20] The slow component observed for low-*J* levels was attributed to roaming, while the broader faster component was attributed to secondary dissociation of internally excited CH_3CO formed *via* channel (I). It is not immediately clear how an intramolecular reaction between nascent CH_3 and CH_3CO radicals could lead to the CO + C_2H_6 products. One possibility is a three-center transition state in which the C–C bonds in the nascent ethane and acetyl, form and break simultaneously. The other is an S_N2-like reaction, although this mechanism is more typically observed in ion–molecule reactions (*e.g.* $Cl^- + CH_3I \rightarrow ClCH_3 + I^-$) in the gas-phase.[59] Kable and co-workers have suggested an analogous mechanism involving H + CH_3CO roaming occurs in acetaldehyde.[40] Formation of $CH_2CO + CH_4$, on the other hand, would require a simple H-atom abstraction, akin to roaming pathways identified in formaldehyde and acetaldehyde.[52–55] Unfortunately, the current measurements do not determine partitioning of E_{INT} between the CH_2CO and CH_4 fragments, and cannot conclusively demonstrate roaming. If roaming is indeed the exclusive route to molecular products, then one would expect that the intramolecular H-atom abstraction reaction between nascent CH_3 and CH_3CO would lead to highly internally excited CH_4, as has been observed for the roaming mechanism in acetaldehyde.[57] Imaging the ketene products using a state-resolved resonant ionization approach[60] would be a potentially insightful measurement, allowing characterization of the correlated internal energy distribution of the CH_4 product. Confirmation that a roaming mechanism is responsible for the ketene-forming channel will require theoretical support.

Conclusions

We have used single-photon universal VUV ionization to detect molecular and radical products of acetone photolysis following excitation to S_1. PHOFEX measurements characterize the relative yields of the radical products, methyl and acetyl, and the molecular product ketene across a broad range of wavelengths. Ketene is formed with non-negligible yield. The observed partitioning of the available energy in ketene determined from ion imaging measurements is incompatible with dissociation over relatively high barriers on S_0, instead a roaming mechanism involving frustrated dissociation to the radical products CH_3 + CH_3CO and subsequent intramolecular H-atom abstraction is proposed. The formation of radical products occurs primarily on the T_1 surface once sufficient energy is available to overcome the barrier, although there is evidence of statistical dissociation on S_0 at longer wavelengths. Picosecond time-resolved imaging at 266 nm reveals that the radical products are formed exclusively on T_1 and characterize the rate of intersystem crossing, which is significantly slower than in acetaldehyde. Slow formation on T_1 at 284 nm is reconciled with a significantly shorter fluorescence lifetime by a proposed two-step mechanism in which the S_0 state acts as a temporary population reservoir, prior to intersystem crossing to the T_1 surface upon which dissociation can occur rapidly.

Conflicts of interest

There are no conflicts to declare.

Acknowledgements

This material is based upon work supported by the National Science Foundation under Grant No. CHE-1566064. CM and BWT are also grateful for support from AirUCI and the Laser Spectroscopy Facility.

References

1 M. Baba and I. Hanazaki, The S_1, $^1A_2(n,\pi^*)$ State of Acetone in a Supersonic Nozzle Beam. Methyl Internal Rotation, *Chem. Phys. Lett.*, 1983, **103**(2), 93–97.
2 M. Baba, I. Hanazaki and U. Nagashima, The $S_1(n,\pi^*)$ States of Acetaldehyde and Acetone in Supersonic Nozzle Beam: Methyl Internal Rotation and C=O Out-of-plane Wagging, *J. Chem. Phys.*, 1985, **82**(9), 3938–3947.
3 J. B. Burkholder, S. P. Sander, J. Abbatt, J. R. Barker, R. E. Huie, C. E. Kolb, M. J. Kurylo, V. L. Orkin, D. M. Wilmouth and P. H. Wine, "Chemical Kinetics and Photochemical Data for Use in Atmospheric Studies, Evaluation No. 18," JPL Publication 15–10, Jet Propulsion Laboratory, Pasadena, 2015, http://jpldataeval.jpl.nasa.gov.
4 D. J. Donaldson and S. R. Leone, Photofragmentation Dynamics of Acetone of 193 nm: State Distributions of the CH_3 and CO Fragments by Time- and Wavelength-resolved Infrared Emission, *J. Chem. Phys.*, 1986, **85**(2), 817–824.

5 P. D. Lightfoot, S. P. Kirwan and M. J. Pilling, Photolysis of Acetone at 193.3 nm, *J. Phys. Chem.*, 1988, **92**(17), 4938–4946.
6 K. A. Trentelman, S. H. Kable, D. B. Moss and P. L. Houston, Photodissociation Dynamics of Acetone at 193 nm: Photofragment Internal and Translational Energy Distributions, *J. Chem. Phys.*, 1989, **91**(12), 7498–7513.
7 G. E. Hall, H. W. Metzler, J. T. Muckerman, J. M. Preses and R. E. Weston, Studies of the 193 nm Photolysis of Diethyl Ketone and Acetone Using Time-resolved Fourier Transform Emission Spectroscopy, *J. Chem. Phys.*, 1995, **102**(17), 6660–6668.
8 S. W. North, D. A. Blank, J. D. Gezelter, C. A. Longfellow and Y. T. Lee, Evidence for Stepwise Dissociation Dynamics in Acetone at 248 and 193 nm, *J. Chem. Phys.*, 1995, **102**(11), 4447–4460.
9 K. Takahashi, T. Nakayama, Y. Matsumi and Y. Osamura, Hydrogen Atom Formation in the Photolysis of Acetone at 193 nm, *J. Phys. Chem. A*, 2004, **108**(39), 8002–8008.
10 R. A. Copeland and D. R. Crosley, Radiative, Collisional and Dissociative Processes in Triplet Acetone, *Chem. Phys. Lett.*, 1985, **115**(4), 362–368.
11 G. M. Breuer and E. K. C. Lee, Fluorescence Decay Times of Cyclic Ketones, Acetone, and Butanal in the Gas Phase, *J. Phys. Chem.*, 1971, **75**(7), 989–990.
12 O. Anner, H. Zuckermann and Y. Haas, Fluorescence Decay of Jet-Cooled Acetone, *J. Phys. Chem.*, 1985, **89**(8), 1336–1339.
13 H. Zuckermann, B. Schmitz and Y. Haas, Dissociation Energy of an Isolated Triplet Acetone Molecule, *J. Phys. Chem.*, 1988, **92**(17), 4835–4837.
14 H. Zuckermann, B. Schmitz and Y. Haas, Acetone Photophysics in Seeded Supersonic Molecular Beams, *J. Phys. Chem.*, 1989, **93**(10), 4083–4091.
15 H. Zuckermann, Y. Haas, M. Drabbels, J. Heinze, W. L. Meerts, J. Reuss and J. van Bladel, Acetone, a Laser-Induced Fluorescence Study with Rotational Resolution at 320 nm, *Chem. Phys.*, 1992, **163**(2), 193–208.
16 Y. Haas, Photochemical α-Cleavage of Ketones: Revisiting Acetone, *Photochem. Photobiol. Sci.*, 2004, **3**(1), 6–16.
17 L. D. Waits, R. J. Horwitz and J. A. Guest, Translational Energy Study of CH_3 Photofragments Following (n,π^*) Excitation of Acetone, *Chem. Phys.*, 1991, **155**(1), 149–156.
18 E. Martínez-Núñez, A. Fernández-Ramos, M. N. D. S. Cordeiro, S. A. Vázquez, F. J. Aoiz and L. Bañares, A Direct Classical Trajectory Study of the Acetone Photodissociation on the Triplet Surface, *J. Chem. Phys.*, 2003, **119**(20), 10618–10625.
19 K. L. K. Lee, K. Nauta and S. H. Kable, Photodissociation of Acetone from 266 to 312 nm: Dynamics of CH_3 + CH_3CO Channels on the S_0 and T_1 States, *J. Chem. Phys.*, 2017, **146**(4), 044304.
20 V. Goncharov, N. Herath and A. G. Suits, Roaming Dynamics in Acetone Dissociation, *J. Phys. Chem. A*, 2008, **112**(39), 9423–9428.
21 S. K. Kim, S. Pedersen and A. H. Zewail, Direct Femtosecond Observation of the Transient Intermediate in the A-cleavage Reaction of $(CH_3)_2CO$ to $2CH_3$ + CO: Resolving the Issue of Concertedness, *J. Chem. Phys.*, 1995, **103**(1), 477–480.
22 W.-K. Chen, J.-W. Ho and P.-Y. Cheng, Ultrafast Photodissociation Dynamics of the Acetone 3*s* Rydberg State at 195 nm: A New Mechanism, *Chem. Phys. Lett.*, 2003, **380**(3–4), 411–418.
23 W.-K. Chen, J.-W. Ho and P.-Y. Cheng, Ultrafast Photodissociation Dynamics of Acetone at 195 nm: I. Initial-State, Intermediate, and Product Temporal Evolutions by Femtosecond Mass-Selected Multiphoton Ionization Spectroscopy, *J. Phys. Chem. A*, 2005, **109**(31), 6805–6817.
24 W.-K. Chen and P.-Y. Cheng, Ultrafast Photodissociation Dynamics of Acetone at 195 nm: II. Unraveling Complex Three-Body Dissociation Dynamics by Femtosecond Time-Resolved Photofragment Translational Spectroscopy, *J. Phys. Chem. A*, 2005, **109**(31), 6818–6829.
25 S. A. Buzza, E. M. Snyder, D. A. Card, D. E. Folmer and A. W. Castleman Jr, Femtosecond Excitation Dynamics of Acetone: Dissociation, Ionization, and the Evolution of Multiply Charged Elemental Species, *J. Chem. Phys.*, 1996, **105**(17), 7425–7431.
26 S. A. Buzza, E. M. Snyder and A. W. Castleman Jr, Further Direct Evidence for Stepwise Dissociation of Acetone and Acetone Clusters, *J. Chem. Phys.*, 1996, **104**(13), 5040–5047.
27 T. Shibata and T. Suzuki, Photofragment Ion Imaging with Femtosecond Laser Pulses, *Chem. Phys. Lett.*, 1996, **262**(1), 115–119.
28 Q. Zhong, L. Poth and A. W. Castleman Jr, Ultrafast Dissociation Dynamics of Acetone: A Revisit to the S_1 State and 3*s* Rydberg State, *J. Chem. Phys.*, 1999, **110**(1), 192–196.
29 J. C. Owrutsky and A. P. Baronavski, Ultrafast Photodissociation Dynamics of the S_1 and S_2 States of Acetone, *J. Chem. Phys.*, 1999, **110**(23), 11206–11213.
30 E. W.-G. Diau, C. Kötting and A. H. Zewail, Femtochemistry of Norrish Type-I Reactions: I. Experimental and Theoretical Studies of Acetone and Related Ketones on the S_1 Surface, *ChemPhysChem*, 2001, **2**(5), 273–293.
31 N. Rusteika, K. B. Møller and T. I. Sølling, New Insights on the Photodynamics of Acetone Excited with 253–288 nm Femtosecond Pulses, *Chem. Phys. Lett.*, 2008, **461**(4–6), 193–197.
32 R. Y. Brogaard, T. I. Sølling and K. B. Møller, Initial Dynamics of The Norrish Type I Reaction in Acetone: Probing Wave Packet Motion, *J. Phys. Chem. A*, 2011, **115**(5), 556–561.
33 H. Sakurai and S. Kato, A Theoretical Study of the Norrish Type I Reaction of Acetone, *J. Mol. Struct.*, 1999, **461**, 145–152.
34 D. Liu, W.-H. Fang and X.-Y. Fu, An *Ab Initio* Study on Photodissociation of Acetone, *Chem. Phys. Lett.*, 2000, **325**(1–3), 86–92.
35 S. Maeda, K. Ohno and K. Morokuma, A Theoretical Study on the Photodissociation of Acetone: Insight into the Slow Intersystem Crossing and Exploration of Nonadiabatic Pathways to the Ground State, *J. Phys. Chem. Lett.*, 2010, **1**(12), 1841–1845.
36 L. Favero, G. Granucci and M. Persico, Dynamics of Acetone Photodissociation: A Surface Hopping Study, *Phys. Chem. Chem. Phys.*, 2013, **15**(47), 20651–20661.
37 B. W. Toulson, K. M. Kapnas, D. A. Fishman and C. Murray, Competing Pathways in the Near-UV Photochemistry of Acetaldehyde, *Phys. Chem. Chem. Phys.*, 2017, **19**(22), 14276–14288.
38 D. Townsend, M. P. Minitti and A. G. Suits, Direct Current Slice Imaging, *Rev. Sci. Instrum.*, 2003, **74**(4), 2530–2539.

39 A. H. Kung, J. F. Young and S. E. Harris, Generation of 1182 Å Radiation in Phase-matched Mixtures of Inert Gases, *Appl. Phys. Lett.*, 1973, **22**(6), 301–302.

40 K. L. K. Lee, M. S. Quinn, A. T. Maccarone, K. Nauta, P. L. Houston, S. A. Reid, M. J. T. Jordan and S. H. Kable, Two Roaming Pathways in the Photolysis of CH_3CHO between 328 and 308 nm, *Chem. Sci.*, 2014, **5**(12), 4633–4638.

41 B. Gans, L. A. V. Mendes, S. Boyé-Péronne, S. Douin, G. Garcia, H. Soldi-Lose, B. K. C. de Miranda, C. Alcaraz, N. Carrasco and P. Pernot, *et al.*, Determination of the Absolute Photoionization Cross Sections of CH_3 and I Produced from a Pyrolysis Source, by Combined Synchrotron and Vacuum Ultraviolet Laser Studies, *J. Phys. Chem. A*, 2010, **114**(9), 3237–3246.

42 B. Yang, J. Wang, T. A. Cool, N. Hansen, S. Skeen and D. L. Osborn, Absolute Photoionization Cross-Sections of Some Combustion Intermediates, *Int. J. Mass Spectrom.*, 2012, **309**, 118–128.

43 D. H. Mordaunt, D. L. Osborn and D. M. Neumark, Non-statistical Unimolecular Dissociation over a Barrier, *J. Chem. Phys.*, 1998, **108**(6), 2448–2457.

44 S. North, D. A. Blank and Y. T. Lee, Determination of the Barrier Height to CH_3CO Dissociation, *Chem. Phys. Lett.*, 1994, **224**(1), 38–42.

45 X. Tang, B. J. Ratliff, B. L. FitzPatrick and L. J. Butler, Determination of the Barrier Height for Acetyl Radical Dissociation from Acetyl Chloride Photodissociation at 235 nm Using Velocity Map Imaging, *J. Phys. Chem. B*, 2008, **112**(50), 16050–16058.

46 B. F. Gherman, R. A. Friesner, T.-H. Wong, Z. Min and R. Bersohn, Photodissociation of Acetaldehyde: The CH_4 + CO Channel, *J. Chem. Phys.*, 2001, **114**(14), 6128–6133.

47 C. L. Berrie, C. A. Longfellow, A. G. Suits and Y. T. Lee, Infrared Multiphoton Dissociation of Acetone in a Molecular Beam, *J. Phys. Chem. A*, 2001, **105**(12), 2557–2562.

48 S. H. Mousavipour and P. D. Pacey, Initiation and Abstraction Reactions in the Pyrolysis of Acetone, *J. Phys. Chem.*, 1996, **100**(9), 3573–3579.

49 H.-J. Werner, P. J. Knowles, G. Knizia, F. R. Manby, M. Schütz, P. Celani, T. Korona, R. Lindh, A. Mitrushenkov, G. Rauhut, K. R. Shamasundar, T. B. Adler, R. D. Amos, A. Bernhardsson, A. Berning, D. L. Cooper, M. J. O. Deegan, A. J. Dobbyn, F. Eckert, E. Goll, C. Hampel, A. Hesselmann, G. Hetzer, T. Hrenar, G. Jansen, C. Köppl, Y. Liu, A. W. Lloyd, R. A. Mata, A. J. May, S. J. McNicholas, W. Meyer, M. E. Mura, A. Nicklass, D. P. O'Neill, P. Palmieri, D. Peng, K. Pflüger, R. Pitzer, M. Reiher, T. Shiozaki, H. Stoll, A. J. Stone, R. Tarroni, T. Thorsteinsson and M. Wang, *MOLPRO, Version 2012.1, a Package of Ab Initio Programs*, see http://www.molpro.net.

50 A. E. Clubb, M. J. T. Jordan, S. H. Kable and D. L. Osborn, Phototautomerization of Acetaldehyde to Vinyl Alcohol: A Primary Process in UV-Irradiated Acetaldehyde from 295 to 335 nm, *J. Phys. Chem. Lett.*, 2012, 3522–3526.

51 D. U. Andrews, B. R. Heazlewood, A. T. Maccarone, T. Conroy, R. J. Payne, M. J. T. Jordan and S. H. Kable, Photo-Tautomerization of Acetaldehyde to Vinyl Alcohol: A Potential Route to Tropospheric Acids, *Science*, 2012, **337**(6099), 1203–1206.

52 A. G. Suits, Roaming Atoms and Radicals: A New Mechanism in Molecular Dissociation, *Acc. Chem. Res.*, 2008, **41**(7), 873–881.

53 N. Herath and A. G. Suits, Roaming Radical Reactions, *J. Phys. Chem. Lett.*, 2011, **2**(6), 642–647.

54 J. M. Bowman and B. C. Shepler, Roaming Radicals, *Annu. Rev. Phys. Chem.*, 2011, **62**, 531–553.

55 J. M. R. Bowman, Roaming, *Mol. Phys.*, 2014, 1–13.

56 D. Townsend, S. A. Lahankar, S. K. Lee, S. D. Chambreau, A. G. Suits, X. Zhang, J. Rheinecker, L. B. Harding and J. M. Bowman, The Roaming Atom: Straying from the Reaction Path in Formaldehyde Decomposition, *Science*, 2004, **306**(5699), 1158–1161.

57 P. L. Houston and S. H. Kable, Photodissociation of Acetaldehyde as a Second Example of the Roaming Mechanism, *Proc. Natl. Acad. Sci. U. S. A.*, 2006, **103**(44), 16079–16082.

58 B. R. Heazlewood, M. J. T. Jordan, S. H. Kable, T. M. Selby, D. L. Osborn, B. C. Shepler, B. J. Braams and J. M. Bowman, Roaming Is the Dominant Mechanism for Molecular Products in Acetaldehyde Photodissociation, *Proc. Natl. Acad. Sci. U. S. A.*, 2008, **105**(35), 12719–12724.

59 J. Mikosch, S. Trippel, C. Eichhorn, R. Otto, U. Lourderaj, J. X. Zhang, W. L. Hase, M. Weidemuller and R. Wester, Imaging Nucleophilic Substitution Dynamics, *Science*, 2008, **319**(5860), 183–186.

60 M. N. R. Ashfold, A. D. Couch, R. N. Dixon and B. Tutcher, Rydberg States of Ketene Revealed by Multiphoton Ionization Spectroscopy, *J. Phys. Chem.*, 1988, **92**(19), 5327–5332.